

# Reversible and Tunable Second-Order Nonlinear Optical Susceptibility in PZT Thin Films for Integrated Optics

Gilles F. Feutmba, Artur Hermans, John P. George, Hannes Rijckaert, Ifan Ansari, Dries Van Thourhout, and Jeroen Beeckman\*

Second-order nonlinear optical processes enable a wide range of applications used in research and industry. The majority of available second-order nonlinear devices however relies on bulk nonlinear crystals with low second-order nonlinearity. By exploiting the advancements made in integrated optics, materials with large second-order nonlinearity can enable efficient and small-sized on-chip nonlinear devices at low cost. Unfortunately, silicon and silicon nitride, mostly used for photonics integrated circuits exhibit negligible second-order nonlinearity ( $\chi^{(2)}$ ) and alternate materials have to be investigated. Lead zirconate titanate (PZT) thin films with high second-order nonlinearity stand as a good candidate for on-chip nonlinearity. An electric-field induced tuning of  $\chi^{(2)}$  is demonstrated here in PZT thin films grown on glass substrates with a tuning efficiency of  $3.35 \text{ pm V}^{-2}$ . Strong second-harmonic generation is recorded and a very high dominant tensor component  $\chi_{zz}^{(2)}$  of  $128 \text{ pm V}^{-1}$  is reported. The  $\chi^{(2)}$  of the PZT thin films can be reversed by poling with a DC electric field at room temperature. This opens avenues for highly efficient and tunable on-chip nonlinear devices.

difference-frequency generation have generated remarkable progress in applications and fields such as ultrafast optical spectroscopy,<sup>[1]</sup> harmonic generation microscopy,<sup>[2]</sup> and quantum computing.<sup>[3]</sup> Frequency-doubled lasers,<sup>[4]</sup> optical parametric oscillators,<sup>[6]</sup> and amplifiers<sup>[8]</sup> and terahertz radiation sources<sup>[9]</sup> are all examples of useful devices that rely on second-order nonlinear effects. Moreover, apart from  $\chi^{(2)}$  based light generation, electro-optic modulators<sup>[10]</sup> based on the Pockels effect are key devices used in our communication world. Most of these devices are however expensive and still rely on bulky nonlinear crystals.

Integrated optics has enabled smaller and power efficient photonic integrated circuits (PICs), mass manufacturable at low cost. The complexity and functionality of these PICs can be greatly improved by integrating the aforementioned nonlinear

devices. By exploiting third-order nonlinearities in silicon (Si) and silicon nitride (SiN) for example, PICs for quantum random number generation,<sup>[11]</sup> wavelength converters,<sup>[12]</sup> and frequency comb generation<sup>[13]</sup> have been demonstrated. Compared to third-order nonlinearities, second-order nonlinearities are stronger and require lower powers. Unfortunately, Si has a centrosymmetric structure and hence does not support second-order nonlinear processes. However, by introducing strain fields in Si waveguides using SiN thin films or by applying DC fields across p–i–n junctions in Si ridge waveguides, an induced  $\chi^{(2)}$  of  $40 \text{ pm V}^{-1}$  at  $2.3 \text{ }\mu\text{m}$  and  $41 \text{ pm V}^{-1}$  at  $2.29 \text{ }\mu\text{m}$  was respectively measured in SHG experiments.<sup>[14]</sup> The complexity in obtaining these  $\chi^{(2)}$  values however still remains an issue. In SiN films deposited using plasma-enhanced chemical vapor deposition (PECVD),  $\chi_{zz}^{(2)}$  values (with z normal to the film plane) up to  $5 \text{ pm V}^{-1}$  at  $1064 \text{ nm}$  were found using SHG experiments.<sup>[16]</sup> The  $\chi^{(2)}$  value obtained is however still low compared to most nonlinear crystals.

The integration of thin films from nonlinear crystals on Si or SiN (heterogeneous integration) has therefore been investigated as an attempt for realizing on-chip optical nonlinear devices. The thin films should have large second-order nonlinearity and high optical quality. Lithium niobate ( $\text{LiNbO}_3$ ) crystals, the golden standard in nonlinear optics for their well-established nonlinear properties stand as a primary material for such integration. They have been extensively used as Pockels based electro-optic modulators in the telecommunication

## 1. Introduction

Second-order nonlinear optical effects such as second-harmonic generation (SHG), parametric down-conversion, and

G. F. Feutmba, Dr. J. P. George, Dr. H. Rijckaert, I. Ansari, Prof. J. Beeckman

Liquid Crystals and Photonics Group  
ELIS Department

Ghent University

Technologiepark-Zwijnaarde, Gent 9052, Belgium

E-mail: jeroen.beeckman@ugent.be

G. F. Feutmba, Dr. A. Hermans, I. Ansari, Prof. D. Van Thourhout

Photonics Research Group

INTEC Department

Ghent University-imec

Technologiepark-Zwijnaarde, Gent 9052, Belgium

G. F. Feutmba, Dr. A. Hermans, Dr. J. P. George, I. Ansari,

Prof. D. Van Thourhout, Prof. J. Beeckman

Center for Nano- and Biophotonics (NB-Photonics)

Ghent University

Technologiepark-Zwijnaarde, Gent 9052, Belgium


Dr. H. Rijckaert

Sol-gel Centre for Research on Inorganic Powders and Thin films

Department of Chemistry

Ghent University

Krijgslaan 281-S3, Gent 9000, Belgium

 The ORCID identification number(s) for the author(s) of this article can be found under <https://doi.org/10.1002/adom.202100149>.

DOI: 10.1002/adom.202100149

industry and the  $\chi^{(2)}$  coefficients have also been investigated through SHG experiments,<sup>[17]</sup> with  $\chi_{zzz}^{(2)} = -54 \text{ pm V}^{-1}$  the largest reported coefficient at 1064 nm.<sup>[18]</sup> Recently, on-chip SHG in periodically poled or nanopatterned LiNbO<sub>3</sub> waveguides bonded on Si or SiO<sub>2</sub> was reported.<sup>[19]</sup> SHG has also been demonstrated in barium titanate (BaTiO<sub>3</sub>) thin films,<sup>[24]</sup> with a stress-induced enhanced  $\chi_{zzz}^{(2)} = 152 \text{ pm V}^{-1}$  measured at 1064 nm from a Ce:BaTiO<sub>3</sub>:SrTiO<sub>3</sub> superlattice.<sup>[24]</sup> However, the heterogenous integration of LiNbO<sub>3</sub> and BaTiO<sub>3</sub> films requires an additional bonding procedure and the optical loss from BaTiO<sub>3</sub> films is high (6 dB cm<sup>-1</sup>).<sup>[27]</sup> Nonlinear organic crystals 4-N, N-dimethylamino-4'-N'-methyl-stilbazolium tosylate (DAST) or N-benzyl-2-methyl-4-nitroaniline (BNA) have also been used for strong second-harmonic generation with  $\chi^{(2)}$  values as high as  $\chi_{xxx}^{(2)} = 580 \text{ pm V}^{-1}$  at 1542 nm and  $\chi_{zzz}^{(2)} = 468 \text{ pm V}^{-1}$  at 1064 nm respectively.<sup>[28]</sup> SHG measurements performed at 1550 nm revealed a  $\chi_{zzz}^{(2)} = 160 \text{ pm V}^{-1}$  in BNA crystals<sup>[30]</sup> and  $\chi_{zzz}^{(2)} = 153 \pm 70 \text{ pm V}^{-1}$  in BNA thin films.<sup>[31]</sup> Although very high  $\chi^{(2)}$  values are reported for these organic crystals, the challenges to grow organic crystalline thin films of high optical quality pose a problem for realizing efficient on-chip nonlinearity.

Amongst ferroelectric oxides, lead zirconate titanate (PZT) has been used for micro-piezoelectric sensors and actuators in micro-electromechanical systems (MEMS), acoustic sensors and nonvolatile random-access memories (NVRAMs) because of its excellent ferroelectric and piezoelectric characteristics.<sup>[32]</sup> The large transparency window<sup>[35]</sup> and optical nonlinearities<sup>[36]</sup> in PZT also position it as a suitable material for on-chip nonlinear devices. A novel approach to integrate thin films of PZT with excellent electrical and optical properties on different substrates has been reported.<sup>[37]</sup> An intermediate low-loss lanthanide-based layer is used as a seed for the PZT deposition, as opposed to the highly absorbing metallic-based seed layers used conventionally, enabling direct deposition of the thin film on top of Si or SiN waveguides. PZT thin films with strong Pockels effect have been successfully grown on SiN<sup>[38]</sup> and Si<sup>[39]</sup> waveguides by using this approach and high speed electro-optic modulation with an additional loss <1 dB cm<sup>-1</sup> was reported. Although SHG has been used to probe ferroelectric PZT films,<sup>[40]</sup> no  $\chi^{(2)}$  values have been reported. The large Pockels coefficient ( $\approx 250 \text{ pm V}^{-1}$ ) measured<sup>[37]</sup> from PZT thin films however indicate the interest of measuring the  $\chi^{(2)}$  for SHG also. In this paper, we demonstrate strong SHG from PZT thin films grown on glass substrates using chemical solution deposition. We extract very large second-order optical nonlinear susceptibility components from the SHG measurements and study the effect of poling on the nonlinear response of the PZT thin films. We demonstrate that the second-order nonlinear components can be tuned and reversed by applying an electric-field across the PZT film. The results obtained are consistent over multiple samples.

## 2. Experimental Section

PZT thin films are grown on indium tin oxide (ITO) on glass substrates by chemical solution deposition (CSD), using a lanthanide-based intermediate layer as reported by George and co-workers.<sup>[37]</sup> The intermediate layer acts both as a barrier layer to

prevent the diffusion of lead (Pb) and as a seed layer for PZT growth. Corning glass substrates (CB-90IN, Delta Technologies) 1.1  $\mu\text{m}$  thick are used, coated with a layer of 20 nm thick ITO which acts as a transparent bottom electrode (sheet resistance 70–100  $\Omega \text{ sq}^{-1}$ ). A 10 nm thick lanthanide-based intermediate layer is then deposited followed by the PZT thin film deposition. Both the intermediate layer and the PZT thin films are deposited by a repeated spin-coating and annealing process which allows control of the film thickness. We use the chemical composition PbZr<sub>0.52</sub>Ti<sub>0.48</sub>O<sub>3</sub> for our PZT thin film. The PZT layer is deposited and annealed at 620 °C for 15 min in a tube furnace under an oxygen ambient. Circular (1 mm radius) ITO electrodes, are then finally deposited as top electrodes on the samples. A via through the PZT film is made by ultrasonic soldering for contacting the bottom ITO electrode. Three different samples with PZT thicknesses 871.9 nm (S1), 885 nm (S2), and 920.7 nm (S3) are fabricated. The thickness is measured by spectroscopic ellipsometry.

For the SHG characterization, we use the measurement technique reported by Hermans et al.<sup>[41]</sup> Figure 1b shows the set-up used for the SHG measurements. The light source is a mode-locked laser (Calmar FPL-03CCFPM) emitting 0.1 ps pulses at a wavelength of 1550 nm, a repetition rate of 20 MHz and 12 mW average power. A polarization beam splitter cube (PBSC) is used to ensure linear polarization of the collimated light beam (3 mm beam diameter ( $1/e^2$ )). A half-wave plate is used to rotate the polarization direction of the linearly polarized light during measurements. The half-wave plate is controlled by a motorized stage and allows for polarization-angle dependent measurements. Two parabolic mirrors of 5 cm focal length are used to focus the laser beam on the sample and to collimate it again after the sample. The focused spot beam diameter on the sample ( $1/e^2$ ) is 30  $\mu\text{m}$ . This gives us a depth of focus of 1 mm for the alignment of the sample in the focal plane and about 176 MW cm<sup>-2</sup> peak intensity. A long-pass filter is placed before the sample to filter out any parasitic SH light generated before the sample while a short-pass filter positioned after the sample suppresses the laser light at the fundamental wavelength and allows only the SH light through. The sample is placed on a motorized rotation stage, which allows to set the angle of incidence. A second PBSC positioned before the detector is used as an analyzer allowing either s- or p- (corresponding to 0° and 90° respectively) polarized SH light through. The SH generated light is captured by a silicon avalanche single photon detector (ID120, ID Quantique). During a measurement, the angle of incidence is fixed and the polarization state of the fundamental light beam is modulated by rotating the half-wave plate. The s- and p- polarized SH power is then recorded as a function of the polarization angle. The set-up is calibrated using a Maker fringe measurement<sup>[41]</sup> of a beta barium borate (BBO) crystal with known second-order nonlinearity (see Figure S2 in the Supporting Information for measurement and fitting result). The values used for the nonlinear susceptibility of BBO at a wavelength of 1550 nm are  $\chi_{xxz}^{(2)} = -0.057 \text{ pm V}^{-1}$ ,  $\chi_{yyy}^{(2)} = 4.162 \text{ pm V}^{-1}$ ,  $\chi_{zxx}^{(2)} = -0.076 \text{ pm V}^{-1}$ ,  $\chi_{zzz}^{(2)} = -0.077 \text{ pm V}^{-1}$ . The BBO crystal (from Eksma Optics) is optically contacted on fused silica. It has a size of 10 mm × 10 mm × 0.065 mm with crystal angles  $\theta = 20.2^\circ$  and  $\phi = 90^\circ$ . The calibration is carried out before and immediately after the  $\chi^{(2)}$  measurement on the PZT sample to avoid the influence of possible laser and optics fluctuations.

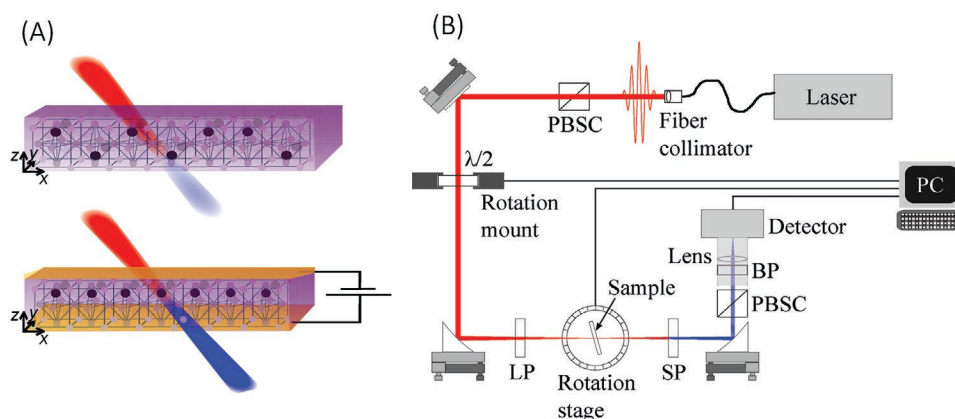


**Figure 1.** A) Schematic of the sample and trajectory of the light beam. Light at the fundamental angular frequency  $\omega$  (in red) excites the sample and light at the SH frequency  $2\omega$  (in blue) exiting the sample is measured. The PZT thin film is poled along the z-direction (picture at the bottom). The black dots are titanium or zirconium ions, whose position define the polarization density of the film. B) Set-up used for the SHG measurements. The sample is mounted on a rotation stage and fixed at 70° incidence. The polarization of the fundamental light is rotated using a half-wave plate on a motorized stage and the s- or p- polarized SH light is measured as a function of polarization angle. Polarization beam splitter cube (PBSC), long-pass filter (LP), short-pass filter (SP), band-pass filter (BP).

After growth, the PZT thin film is polycrystalline with the ferroelectric domains preferentially oriented along the (100) plane as seen in transmission electron microscopy (TEM, **Figure 2a**) and X-ray diffraction (XRD, **Figure 3a**) measurements. Figure 2c and the XRD pattern indicates that the lanthanide-based intermediate layers have a strong preferential growth with the *c*-axis perpendicular to the substrate. This imposes a *c*-axis oriented growth of the PZT thin films (Figure 2b).<sup>[37]</sup> Based on cross-sectional microstructural study, the PZT thin film crystallizes heterogeneously from the lanthanide-based intermediate layer with the formation of a columnar perovskite phase (grain size between 40 and 110 nm) and with the formation of some secondary phases (dark spots in Figure 2a). The lanthanide-based intermediate layer with composition  $\text{La}_2\text{O}_2\text{CO}_3$  acts both as a barrier layer to prevent the diffusion of lead and as a seed

layer for the PZT growth. To estimate the quality of the intermediate layer as barrier layer, elemental distribution maps were obtained (Figure S3, Supporting Information). No lead diffusion from the PZT film to the substrate is observed, indicating that the  $\text{La}_2\text{O}_2\text{CO}_3$  thin layer acts as an efficient buffer layer. The PZT film has a random in-plane orientation<sup>[37]</sup> and thus has a  $C_{\infty v}$  symmetry with respect to the normal and the nonzero second-order susceptibility tensor components are therefore  $\chi_{xxz}^{(2)} = \chi_{yyz}^{(2)} = \chi_{zzx}^{(2)} = \chi_{zyy}^{(2)}$ ,  $\chi_{zxx}^{(2)} = \chi_{zyy}^{(2)}$  and  $\chi_{zzz}^{(2)}$ , where *z* is the film normal and *x* and *y* are the two orthogonal in-plane directions (Figure 1a).<sup>[42]</sup> The values of the second-order susceptibility tensor components calculated here are effective (average) values resulting from the cumulative response of the different domains in the PZT film. To probe the different tensor components, the angle of incidence is set at 70° during

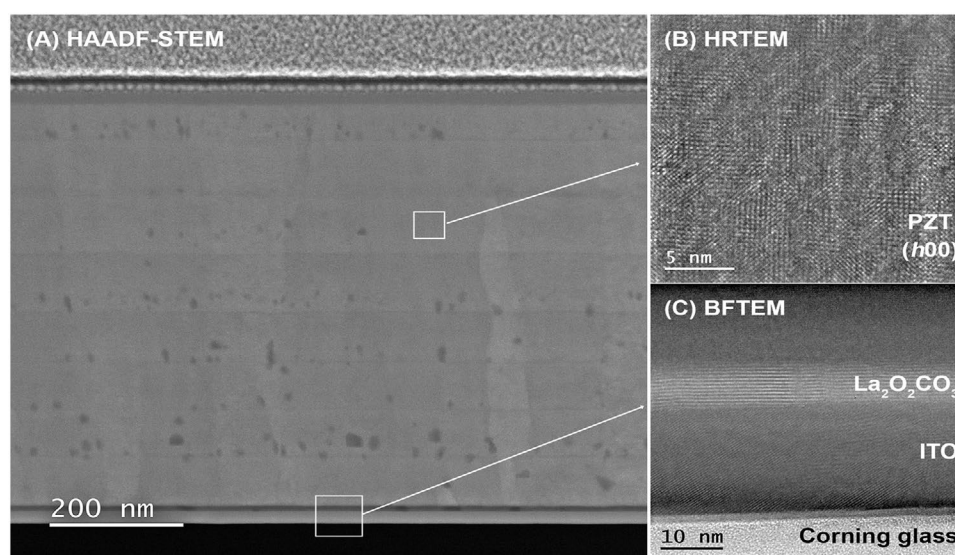


**Figure 2.** A) Scanning transmission electron microscopy (STEM) image of PZT thin film grown on a lanthanide-based intermediate layer deposited on ITO/Corning glass. B) High-resolution (HR) TEM image of grown PZT thin film and C) bright-field (BF) TEM image of the lanthanide-based intermediate layer on ITO.

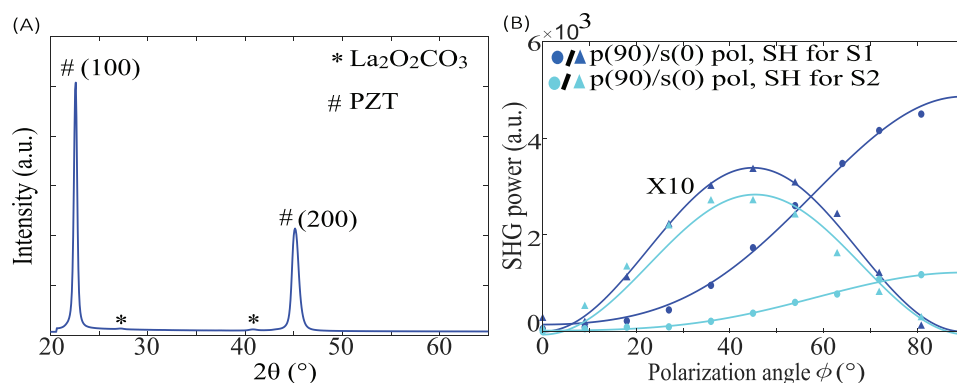


**Figure 3.** A) XRD pattern of PZT thin film grown on glass substrate using a lanthanide-based intermediate layer. B) p- (circles) and s- (triangles) polarized SH power and corresponding fit as a function of the polarization angle obtained from samples S1 and S2 without poling. The nonzero response confirms symmetry breaking after growth. Data and fit of s-polarized SH power is multiplied by 10 for better visibility.

the measurements. The s- and p-polarized SH power are measured and fitted simultaneously to extract the tensor components. The measurement data is fitted to the model described by Bethune<sup>[43]</sup> taking into account reflections in the thin films (see Supporting Information for details about the model and fitting functions). The model is based on an optical transfer matrix formalism. As input, we use the thicknesses and refractive indices of the different layers and we fit the unknown  $\chi^{(2)}$  coefficients. We neglect the weak reflections in the thick glass substrate and the weak SH contribution from the glass–air interface at the back of the substrate.<sup>[41]</sup>

### 3. Results and Discussions

The first measurements are performed on the samples S1 and S2 without prior poling. Figure 3b shows independent measurements of the s- (triangles) and p- (circles) polarized SH power and the corresponding fitted model (lines) as a function of  $\phi$ . The excellent fit indicates that the  $C_{\infty v}$  symmetry is a valid assumption. The results show a nonzero response which indicates that a symmetry breaking in the PZT film is obtained during growth. The ferroelectric domains not only have a preferential (100) out-of-plane orientation after growth, the dipole orientation of the ferroelectric domains is not evenly pointing

towards or away from the substrate, and one of the two directions is dominating. The polarization density in the PZT thin films as obtained after growth varies from sample to sample and this explains the difference observed in Figure 3b for samples S1 and S2.

To maximize the nonlinear response, the samples are poled at room temperature and atmospheric pressure by applying a DC electric field across the PZT film using the ITO electrodes. We performed a measurement where the sample is excited with p-polarized light and we recorded the p-polarized SH power generated while a DC bias is applied across the PZT thin film. **Figure 4** shows the generated SH power, which exhibits a butterfly-like hysteresis behavior. This confirms the ferroelectric nature of the deposited PZT-layer and realignment of the domains with the applied DC field. A slight asymmetry is also visible in the figure as the SH value recorded at  $-15$  V applied voltage is higher than the one at  $+15$  V. This slight difference is again an indication of the preferential alignment of the ferroelectric domains in the direction of growth, i.e., upwards. Furthermore, in Figure 4a we observe an increase in the initial SH generated power with a negative DC bias and a decrease with a positive DC bias (Figure 4b), i.e., electric-field lines downwards, opposing the polarization density. This confirms the preferential alignment of the ferroelectric domains in the direction of growth as a negative bias, i.e., electric-field

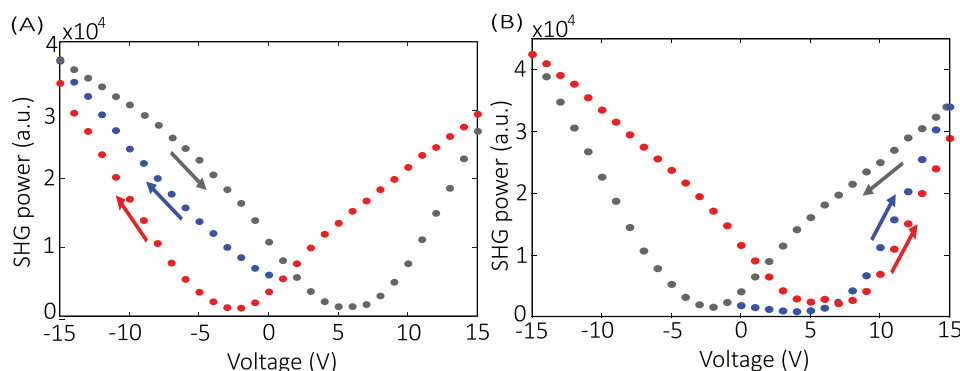


**Figure 4.** Evolution of the SHG power with a triangular DC bias. Starting from 0 V, we apply a DC bias following the blue curve, then gray and finally red. A) Starting from 0 V, we go in the negative bias direction. B) Starting from 0 V, we go in the positive bias. The butterfly hysteresis behavior observed from SH power with DC bias confirms the alignment of the domains and the ferroelectric nature of the PZT thin film.



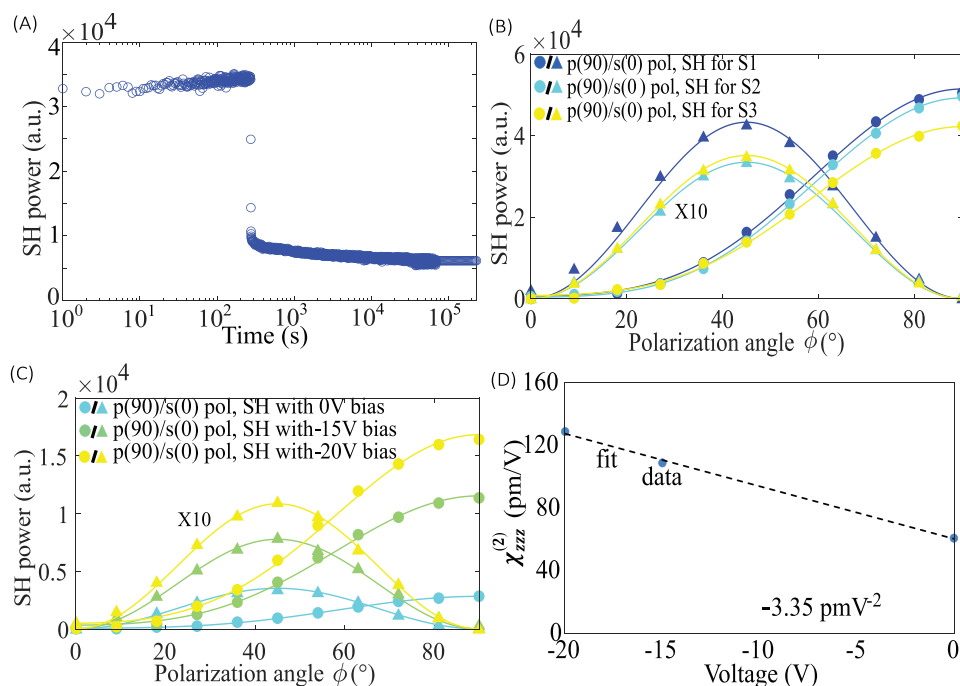


**Figure 5.** A) Time dependent measurement of the SH power during and after poling. B) p- (circles) and s- (triangles) polarized SH power and corresponding fitting curves as a function of the polarization angle obtained from three different samples S1 (blue), S2 (green), S3 (yellow) after poling with -15 V for 10 min. C) SHG power for sample S3 under three biasing conditions; 0 V (blue), -15 V (green), -20 V (yellow). Data and fit of s-polarized SH power is multiplied by 10 for better visibility. D) Evolution of  $\chi_{zzz}^{(2)}$  with increasing bias voltage, including linear fit. Data (blue dots), fit (dotted line).

lines upwards, is in the direction of polarization density while a positive bias opposes the polarization density. The SH power does not appreciably change over time with an applied voltage. Upon release of the applied voltage, the SH power drops to a lower value and then stays stable over a long time (Figure 5a). The measurement is also performed for multiple cycles (see Figure S4 in the Supporting Information). The increase and drop in SH power with and without voltage respectively is attributed to domain switching in the thin film. Figure 5b shows independent measurements of the s- and p-polarized SH power and the corresponding fitted model as a function of  $\phi$  obtained for the three samples after poling with -15 V for 10 min. The measurements are performed with no DC bias and  $\chi_{zzz}^{(2)}$  of 61.1, 60.2, and 59.6 pm V<sup>-1</sup> are obtained for the samples S1, S2 and S3 respectively. Similar  $\chi_{zzz}^{(2)}$  values are obtained irrespective of the poling direction. This similarity in  $\chi_{zzz}^{(2)}$  and hysteresis measurement indicates that the sign of these tensor elements can be reversed with bias voltage, although only the absolute values of the second-order susceptibility tensor components for SHG are extracted here. This opens the way for on-demand domain engineering using applied electric fields. Periodic poling to achieve quasi-phase matching with PZT thin films should thus be possible by careful electrode design. This will therefore lead to higher conversion efficiencies as compared to modal phase matching techniques where the SH is generated in higher order modes and need to be converted back using mode converters. Furthermore, the poling of our PZT films does not require a complicated process and high voltages as used to fabricate periodically poled lithium niobate (PPLN) thin films. Figure 5c shows the measurement of the s- and

p-polarized SH power and the corresponding fitted model as a function of  $\phi$  obtained from sample S3 with three different bias voltages (0, -15, and -20 V). Similar results were obtained with the angle of incidence set at 65° (see Figure S5 in the Supporting Information). The calculated effective  $\chi_{zzz}^{(2)}$  is plotted against applied bias voltage in Figure 5d, from which a linear increase in  $\chi_{zzz}^{(2)}$  with increasing bias voltage is observed. A tuning efficiency of -3.35 pm V<sup>-2</sup> is obtained with an effective  $\chi_{zzz}^{(2)}$  of 128 pm V<sup>-1</sup> measured at -20 V bias. Table 1 below summarizes the extracted tensor components averaged over the three samples.

In the presence of an electric field, the second-order polarization can be described by

$$\mathbf{P}_{2\omega}^{(2)}(r) \propto \chi^{(2)}(-2\omega; \omega, \omega) | \mathbf{E}_{\omega}(r) \mathbf{E}_{\omega}(r) + \chi^{(3)}(-2\omega; \omega, \omega, 0) E_{DC} | \mathbf{E}_{\omega}(r) \mathbf{E}_{\omega}(r) \quad (1)$$

**Table 1.** The average absolute calibrated values of second-order susceptibility tensor components in the PZT film in different bias regimes for three different samples with the corresponding standard deviation.

$\chi^{(2)}$ [pm V <sup>-1</sup> ]	Before poling	After poling, 0 V bias	-15 V bias	-20 V bias
$\chi_{zzz}^{(2)}$	5.6 ± 2.5	60 ± 0.6	108 ± 1.2	128 ± 1.5
$\chi_{xxz}^{(2)}$	0.9 ± 0.2	3.3 ± 0.02	6.1 ± 0.1	7.1 ± 0.4
$\chi_{zxx}^{(2)}$	0.5 ± 0.2	1.7 ± 0.15	4.7 ± 0.04	5.8 ± 0.3

The SHG intensity from this polarization can be described by

$$I_{2\omega} \propto \left[ \left( \chi^{(2)}(-2\omega; \omega, \omega) + \chi^{(3)}(-2\omega; \omega, \omega, 0) E_{\text{DC}} \right) E_{\omega}^2 \right]^2 \quad (2)$$

$$= \left[ \left( \chi^{(2)}(-2\omega; \omega, \omega)^2 + 2\chi^{(2)}(-2\omega; \omega, \omega) \chi^{(3)}(-2\omega; \omega, \omega, 0) E_{\text{DC}} + \left( \chi^{(3)}(-2\omega; \omega, \omega, 0) E_{\text{DC}} \right)^2 \right) E_{\omega}^4 \right] \quad (3)$$

with  $\chi^{(3)}(-2\omega; \omega, \omega, 0) E_{\text{DC}}$  describing a field-dependent effect known as electric-field induced second-harmonic generation (EFISH).<sup>[48]</sup> EFISH is an instantaneous, third-order nonlinear effect that arises from the interaction between the electric field of two photons at frequency  $\omega$  and an external bias at lower frequency. In materials with inversion symmetry the second-order susceptibility is zero and hence only the EFISH contribution remains.<sup>[49]</sup> The SHG power measured in materials without inversion symmetry under a DC bias is therefore a result of the common  $\chi^{(2)}$  SHG process, EFISH and a coupling between the two effects described by the term  $\chi^{(2)}(-2\omega; \omega, \omega) \chi^{(3)}(-2\omega; \omega, \omega, 0) E_{\text{DC}}$  in Equation (2).<sup>[50]</sup> The contribution of these different effects to the field-dependent measurements is ambiguous. We attempt to shed light on the dominant effect at play. Firstly, the hysteretic behavior of the SHG under a DC bias (Figure 4) is associated to the ferroelectric domain switching in the PZT thin film. This domain switching changes the effective  $\chi^{(2)}$  in the PZT thin film, both in terms of the sign and the amplitude. A larger  $\chi^{(2)}$  value is obtained when more domains are aligned along the direction of the DC electric field. The hysteretic behavior however cannot exclude an EFISH contribution in the field-dependent measurements as the coupling term can also induce hysteresis. The influence of the ferroelectric domains switching and relaxing is also seen in the dependence of the SHG power on the DC field. The fitting of the SHG power (see Figure S6 in the Supporting Information) shows a quadratic dependence for low absolute values of the applied electric field (subcoercive field) which could indicate a dominant EFISH effect. However, for larger absolute values of the DC electric field, the SHG power deviates from the quadratic fit and a fairly linear relation with the applied DC field can be observed, which rules out a dominant EFISH contribution. This is consistently observed in the down cycle when the DC electric field is reduced. In a cycle where the DC field is reduced, the ferroelectric domains which had been previously aligned by a larger field are first in a relaxation regime, in which they rotate to a stable population state. Rotation polarization may occur due to the fact that the orientation of the different grains is not perfectly along the direction perpendicular to the substrate. It was recently demonstrated that polarization rotation is an important effect in PZT thin films.<sup>[51]</sup> This is subsequently followed by domain flipping with the DC field around the coercive field. We assume that this change of regime in the hysteresis loop causes the SHG power to deviate from a quadratic dependence on the DC field. The dominant effect at play in the field-dependent measurements thus seems to be associated with domain flipping and reorienting and an effective  $\chi^{(2)}$  change. Also, Bao

et al. measured a rise time of 10 ps for the EFISH response in lead lanthanum zirconate titanate (PLZT)<sup>[52]</sup>, attributing the field-dependent second harmonic generation to symmetry changes and not the pure electronic  $\chi^{(3)}(-2\omega; \omega, \omega, \omega)$  effect, which occurs at fs time scale. While this does not completely exclude the contribution of EFISH in our measurements, it is another indication that the observed SHG effect predominantly originates from a  $\chi^{(2)}$  contribution.

## 4. Conclusions

In conclusion, strong SHG is demonstrated from PZT thin films grown on glass substrates by chemical solution deposition. A thin and low-loss lanthanide layer is used as seed layer and the PZT films can also be easily integrated with Si or SiN photonics integrated circuits as recently demonstrated.<sup>[38]</sup> We were able to confirm symmetry breaking in the PZT thin film after growth with a preferential alignment of the ferroelectric domains in the direction of growth. An average  $\chi_{zzz}^{(2)}$  of 60 pm V<sup>-1</sup> was consistently measured over three different samples after poling. The samples were poled at room temperature and atmospheric pressure. We demonstrated an electric-field induced tuning of the  $\chi^{(2)}$ . A tuning efficiency of -3.35 pm V<sup>-2</sup> is obtained with an effective  $\chi_{zzz}^{(2)}$  of 128 pm V<sup>-1</sup> measured at -20 V bias. This is two times larger than the  $\chi_{zzz}^{(2)}$  of LiNbO<sub>3</sub>. Poling measurements also revealed the reversibility of the  $\chi^{(2)}$  tensor components with a DC bias. This is the first report of such  $\chi^{(2)}$  tuning and reversibility in nonlinear thin films. This positions our PZT thin films as an ideal candidate for new functionalities in thin films and integrated optics such as on-chip optical parametric oscillators, frequency comb generators,<sup>[44]</sup> terahertz sources,<sup>[45]</sup> quantum sources,<sup>[46]</sup> and frequency converters.<sup>[47]</sup>

## Supporting Information

Supporting Information is available from the Wiley Online Library or from the author.

## Acknowledgements

Gilles Freddy Feutmba acknowledges support and funding as an SB-PhD Fellow of the research foundation-Flanders (FWO, Grant number 1S68218N). Hannes Rijckaert acknowledges support and funding as postdoctoral fellow fundamental research of the Research Foundation – Flanders (FWO, Grant number 1273621N). The authors thank Prof. S. Clemmen for his support with the experimental set-up.

## Conflict of Interest

The authors declare no conflict of interest.

## Data Availability Statement

The data that support the findings of this study are available from the corresponding author upon reasonable request.

## Keywords

electric-field-induced tuning, lead zirconate titanate, reversible second-order nonlinearity, second-harmonic generation, thin films

Received: January 27, 2021

Revised: March 26, 2021

Published online:

- [1] M. Maiuri, M. Garavelli, G. Cerullo, *J. Am. Chem. Soc.* **2020**, *142*, 3.
- [2] L. Hyungsik, *Front. Mol. Biosci.* **2019**, *6*, 99.
- [3] A. Belsley, T. Pertsch, F. Setzpfandt, *Opt. Express* **2020**, *28*, 28792.
- [4] A. E. Jalkh, K. Pflibsen, O. Pomerantzeff, C. L. Trempe, C. L. Schepens, *Arch. Ophthalmol.* **1988**, *106*, 847.
- [5] S. J. Herr, V. Brasch, J. Szabados, E. Obrzud, Y. Jia, S. Lecomte, K. Buse, I. Breunig, T. Herr, *Opt. Lett.* **2018**, *43*, 5745..
- [6] APE, GHz Optical Parametric Oscillator (OPO), <https://www.ape-berlin.de/en/opo-optical-parametric-oscillator/opo-x-ghz-fs/> (accessed: December 2020).
- [7] Y. Yamamoto, K. Aihara, T. Leleu, K. Kawarabayashi, S. Kako, M. Fejer, K. Inoue, H. Takesue, *npj Quantum Inf.* **2017**, *3*, 49.
- [8] APE, AVUS Optical Parametric Amplifier (OPA) Provides Widely Tunable High-Energy Pulses, <https://www.ape-berlin.de/en/opa-optical-parametric-amplifier/> (accessed: December 2020).
- [9] Rainbow photonics, TeraTune® a tunable narrowband terahertz source based on a flash lamp pumped laser (repetition rate 50 Hz to 200 Hz) with a special optical parametric oscillator (OPO), [http://www.rainbowphotonics.com/prod\\_teratune.php](http://www.rainbowphotonics.com/prod_teratune.php) (accessed: December 2020).
- [10] Jenoptik, modulators based on electro-optical crystals and make use of Pockels effect, <https://www.jenoptik.com/products/optoelectronic-systems/light-modulation/integrated-optical-modulators-fiber-coupled> (accessed: December 2020).
- [11] Y. Okawachi, M. Yu, K. Luke, D. O. Carvalho, M. Lipson, A. L. Gaeta, *Opt. Lett.* **2016**, *41*, 4194.
- [12] X. Lu, G. Moille, Q. Li, D. A. Westly, A. Singh, A. Rao, S. Yu, T. C. Briles, S. B. Papp, K. Srinivasan, *Nat. Photonics* **2019**, *13*, 593.
- [13] A. L. Gaeta, M. Lipson, T. J. Kippenberg, *Nat. Photonics* **2019**, *13*, 158.
- [14] M. Cazzanelli, F. Bianco, E. Borga, G. Pucker, M. Ghulinyan, E. Degoli, E. Luppi, V. Vénier, S. Ossicini, D. Modotto, S. Wabnitz, R. Pierobon, L. Pavesi, *Nat. Mater.* **2011**, *11*, 148.
- [15] E. Timurdogan, C. V. Poulton, M. J. Byrd, M. R. Watts, *Nat. Photonics* **2017**, *11*, 200.
- [16] K. Koskinen, R. Czaplicki, A. Slablab, T. Ning, A. Hermans, B. Kuyken, V. Mittal, G. S. Murugan, T. Niemi, R. Baets, M. Kauranen, *Opt. Lett.* **2017**, *42*, 5030.
- [17] R. C. Miller, W. A. Nordland, *J. Appl. Phys.* **1971**, *42*, 4145.
- [18] D. A. Roberts, *IEEE J. Quantum Electron.* **1992**, *28*, 2057.
- [19] C. Wang, X. Xiong, N. Andrade, V. Venkataraman, X. F. Ren, G.-C. Guo, M. Lončar, *Opt. Express* **2017**, *25*, 6963.
- [20] R. Luo, Y. He, H. Liang, M. Li, Q. Lin, *Optica* **2018**, *5*, 1006.
- [21] J. Lu, J. B. Surya, X. Liu, A. W. Bruch, Z. Gong, Y. Xu, H. X. Tang, *Optica* **2019**, *6*, 1455.
- [22] A. Rao, M. Malinowski, A. Honardoost, J. R. Talukder, P. Rabiei, P. Delfyett, S. Fathpour, *Opt. Express* **2016**, *24*, 29941.
- [23] Z. Hao, L. Zhang, W. Mao, A. Gao, X. Gao, F. Gao, F. Bo, G. Zhang, J. Xu, *Photon. Res.* **2020**, *8*, 311.
- [24] T. Zhao, H. Lu, F. Chen, G. Yang, Z. Chen, *J. Appl. Phys.* **2000**, *87*, 7448.
- [25] P. T. Lin, B. W. Wessels, J. I. Jang, J. B. Ketterson, *Appl. Phys. Lett.* **2008**, *92*, 221103.
- [26] J. Zhou, W. Zhang, M. Liu, P. T. Lin, *Photon. Res.* **2019**, *7*, 1193.
- [27] F. Eltes, D. Caimi, F. Fallegger, M. Sousa, E. O'Connor, M. D. Rossell, B. Offrein, J. Fompeyrine, S. Abel, *ACS Photonics* **2016**, *3*, 1698.
- [28] M. Jazbinsek, L. Mutter, P. Gunter, *IEEE J. Sel. Top. Quantum Electron* **2008**, *14*, 1298.
- [29] M. Fujiwara, M. Maruyama, M. Sugisaki, H. Takahashi, S. I. Aoshima, R. J. Cogdell, H. Hashimoto, *Jpn. J. Appl. Phys.* **2007**, *46*, 1528.
- [30] T. Notakel, presented at 43rd Int. Conf. on Infrared, Millimeter, and Terahertz Waves (IRMMW-THz), Nagoya, September **2018**.
- [31] A. Hermans, presented at 21st European Conf. on Integrated Optics, Ghent, April **2019**.
- [32] D. Dimos, *Annu. Rev. Mater. Sci.* **1995**, *25*, 273.
- [33] I. Kanno, H. Kotera, K. Wasa, *Sens. Actuators, A* **2003**, *107*, 68.
- [34] N. Izyumskaya, Y.-I. Alivov, S.-J. Cho, H. Morkoç, H. Lee, Y.-S. Kang, *Crit. Rev. Solid State Mater. Sci.* **2007**, *323*, 111.
- [35] S. Samanta, V. Sankaranarayanan, K. Sethupathi, *Vacuum* **2018**, *156*, 456.
- [36] S. Abel, J. Fompeyrine, in *Thin Films on Silicon* (Eds: V. Narayanan, M. M. Frank, A. A. Demkov), Vol. 8, World Scientific, Singapore **2016**, Ch. 10.
- [37] J. P. George, P. F. Smet, J. Botterman, V. Bliznuk, W. Woestenborghs, D. Van Thourhout, K. Neyts, J. Beeckman, *ACS Appl. Mater. Interfaces* **2015**, *7*, 13350.
- [38] K. Alexander, J. P. George, J. Verbist, K. Neyts, B. Kuyken, D. Van Thourhout, J. Beeckman, *Nat. Commun.* **2018**, *9*, 3444.
- [39] G. F. Feutmba, T. Van de Veire, I. Ansari, J. P. George, D. Van Thourhout, J. Beeckman, in *Proc. 2020 OSA Advanced Photonics Congress* (Eds: L. Caspani, A. Tauke-Pedretti, F. Leo, B. Yang), OSA Technical Digest, Washington DC, USA **2020**, paper ITu1A.6.
- [40] J. Nordlander, G. De Luca, N. Strkalj, M. Fiebig, M. Trassin, *Appl. Sci.* **2018**, *8*, 570.
- [41] A. Hermans, C. Kieninger, K. Koskinen, A. Wickberg, E. Solano, J. Dendooven, M. Kauranen, S. Clemmen, M. Wegener, C. Koos, R. Baets, *Sci. Rep.* **2017**, *7*, 44581.
- [42] P. F. Brevet, *Surface Second Harmonic Generation*, Presses Polytechniques et Universitaires Romandes, Lausanne, Switzerland **1997**.
- [43] D. S. Bethune, *J. Opt. Soc. Am. B* **1991**, *8*, 367.
- [44] M. Kues, C. Reimer, J. M. Lukens, W. J. Munro, A. M. Weiner, D. J. Moss, R. Morandotti, *Nat. Photonics* **2019**, *13*, 170.
- [45] K. Lee, J. Park, B. J. Kang, W. T. Kim, H.-D. Kim, S. Baek, K. J. Ahn, B. Min, F. Rotermund, *Adv. Opt. Mater.* **2020**, *8*, 2000359.
- [46] H. Jin, F. M. Liu, P. Xu, J. L. Xia, M. L. Zhong, Y. Yuan, J. W. Zhou, Y. X. Gong, W. Wang, S. N. Zhu, *Phys. Rev. Lett.* **2014**, *113*, 103601.
- [47] D. M. Lukin, C. Dory, M. A. Guidry, K. Y. Yang, S. D. Mishra, R. Trivedi, M. Radulaski, S. Sun, D. Vercruysse, G. H. Ahn, J. Vučković, *Nat. Photonics* **2020**, *14*, 330.
- [48] R. W. Terhune, P. D. Maker, C. M. Savage, *Phys. Rev. Lett.* **1962**, *8*, 404.
- [49] R. W. Boyd, *Nonlinear Optics*, 2nd ed., Academic Press, Cambridge, Massachusetts **2002**.
- [50] S. Chen, K. F. Li, G. Li, K. W. Cheah, S. Zhang, *Light: Sci. Appl.* **2019**, *8*, 17.
- [51] P. Lucke, M. Bayraktar, Y. A. Birkhölzer, M. Nematollahi, A. Yakshin, G. Rijnders, F. Bijkerk, E. P. Houwman, *Adv. Funct. Mater.* **2020**, *30*, 2005397.
- [52] C. Bao, J. C. Diels, *Opt. Lett.* **1995**, *20*, 2186.